ADVANCED ENERGY MATERIALS
www.advenergymat.de

Holistic Strategies Lead to Enhanced Efficiency and Stability of Hybrid Chemical Vapor Deposition Based Perovskite Solar Cells and Modules

*Guoqing Tong, Jiahao Zhang, Tongle Bu, Luis K. Ono, Congyang Zhang, Yuqiang Liu, Chenfeng Ding, Tianhao Wu, Silvia Mariotti, Said Kazaoui, and Yabing Qi**

Hybrid chemical vapor deposition (HCVD) is a promising method for the up-scalable fabrication of perovskite solar cells/modules (PSCs/PSMs). However, the efficiency of the HCVD-based perovskite solar cells still lags behind the solution-processed PSCs/PSMs. In this work, the oxygen loss of the electron transport layer of SnO_2 in the HCVD process and its negative impact on solar cell device performance are revealed. As the counter-measure, potassium sulfamate (H_2KNO_3S) is introduced as the passivation layer to both mitigate the oxygen loss issue of SnO_2 and passivate the uncoordinated Pb^{2+} in the perovskite film. In parallel, *N*-methylpyrrolidone (NMP) is used as the solvent to dissolve PbI_2 by forming the intermediate phase of PbI_2•NMP, which can greatly lower the energy barrier for perovskite nucleation in the HCVD process. The perovskite seed is employed to further modulate the kinetics of perovskite crystal growth and improve the grain size. The resultant solar cells yield a champion power conversion efficiency (PCE) of 21.98% (0.09 cm^2) with a stable output performance of 21.15%, and the PCEs of the mini-modules are 16.16% (22.4 cm^2, stable output performance of 14.72%) and 12.12% (91.8 cm^2). Furthermore, the unencapsulated small area device shows an outstanding operational stability with a T_{80} lifetime exceeding 4000 h.

1. Introduction

In the past decade, tremendous efforts have been made in developing perovskite solar cells (PSCs), which deliver a record power conversion efficiency (PCE) of 25.7%.[1–5] Solution-processed deposition presents a facile, controllable, and versatile technique to fabricate high-quality perovskite films, which are widely used and generate high-performance PSC devices.[6–9] As an alternative technique, vapor-based deposition provides a uniform and dense perovskite (PVSK) film, with less influence from solvents and easy integration with commercial thin film photovoltaic manufacturing.[10–14] Vapor-based deposition methods commonly include co-evaporation deposition,[10,15,16] sequential vapor deposition,[17–21] and hybrid chemical vapor deposition (HCVD).[22–24] The co-evaporation method is carried out by simultaneously sublimating the precursor materials such as PbI_2 and methylammonium iodide (MAI) or formamidinium iodide (FAI) in a high vacuum equipment, which has been demonstrated as an efficient technique to fabricate the highly uniform perovskite films. Similarly, the sequential vapor deposition is processed by sequential deposition of PbI_2 and MAI/FAI/CsX (X = I, Br, Cl) in a high vacuum system, which is expected to avoid the difficulty in

G. Tong, J. Zhang, T. Bu, L. K. Ono, C. Zhang, Y. Liu, C. Ding, T. Wu, S. Mariotti, Y. Qi
Energy Materials and Surface Sciences Unit (EMSSU)
Okinawa Institute of Science and Technology Graduate University (OIST)
1919-1 Tancha, Onna-son, Kunigami-gun, Okinawa 904-0495, Japan
E-mail: yabing.qi@oist.jp

The ORCID identification number(s) for the author(s) of this article can be found under https://doi.org/10.1002/aenm.202300153

DOI: 10.1002/aenm.202300153

G. Tong
School of Materials Science and Engineering
Hefei University of Technology
Hefei 230009, P. R. China

T. Bu
State Key Laboratory of Advanced Technology for Materials Synthesis and Processing
Wuhan University of Technology
Wuhan 430070, P. R. China

Y. Liu
College of Textiles & Clothing
State Key Laboratory of Bio-fibers and Eco-textiles
Qingdao University
Qingdao 266071, P. R. China

S. Kazaoui
Department of Energy and Environment
National Institute of Advanced Industrial Science and Technology (AIST)
Tsukuba, Ibaraki 305-8568, Japan

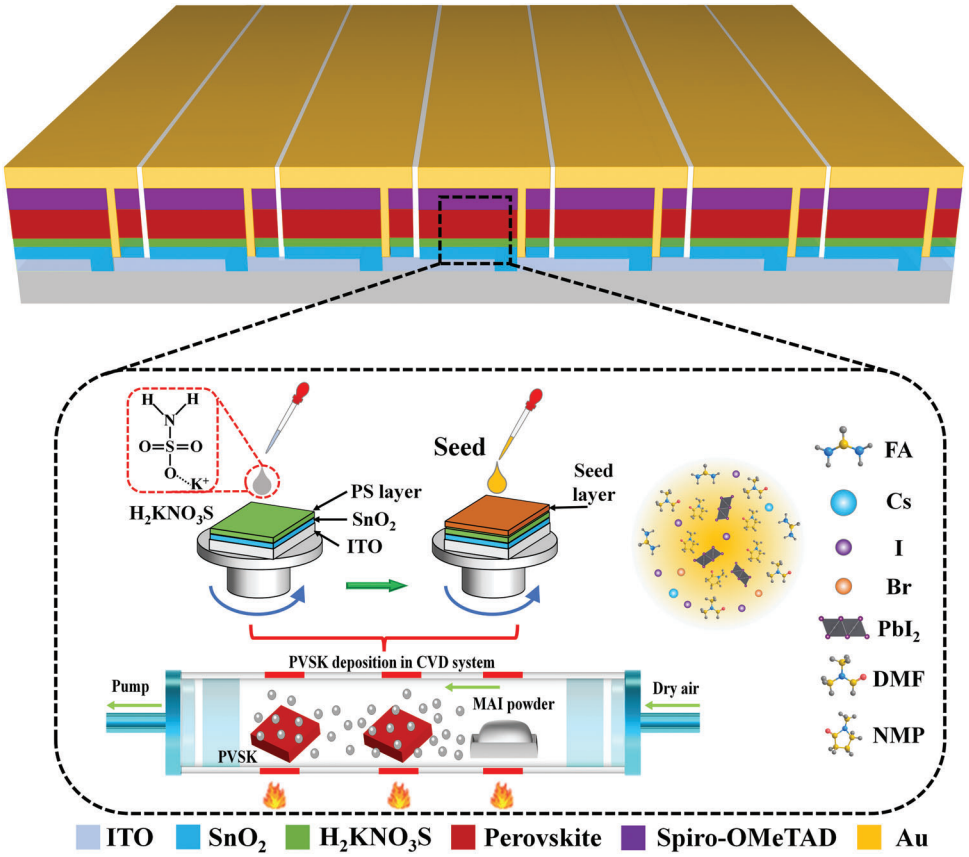

Figure 1. Schematic illustration of a HCVD based perovskite solar cell. Note that here the PbI_2 film reacting with partial FAI is named as Seed.

simultaneously controlling the evaporation rate, yielding a high-quality and uniform perovskite film.[25] The high vacuum deposition method, however, increases the cost in the large-area manufacturing and mass production.[26] Alternatively, HCVD is a feasible way to overcome the aforementioned shortcomings by substituting the high vacuum system with a relative low vacuum equipment.[26] Moreover, HCVD process is a mature and low-cost technique and has been successfully demonstrated in the amorphous Si photovoltaic industry, which enables fabrication of highly uniform thin films with an area over 1 m^2.[26,27]

Compared with the solution-processed perovskites, the performance of HCVD-based PSCs is still inferior to those fabricated using the solution process. Previous reports have demonstrated that the long-term vacuum treatment in HCVD can damage the electron transport layer (ETL) in PSCs with the n–i–p structure, which not only reduces the carrier transport but also increases the defect density at the ETL/PVSK interface, leading to a poor efficiency.[28–30] Some additional buffer layers such as C_{60}, [6,6]-phenyl-C61-butyric acid methyl ester (PCBM), triphenylphosphine oxide (TPPO), and K_2SO_4 have been shown to protect the ETL (i.e., SnO_2 and TiO_2).[28,29,31,32] However, the efficiency of the resultant devices still lags behind the solution process. In addition, the growth of the perovskite films highly depends on the solid–gas reaction in HCVD instead of liquid phase reaction in the case of the solution process. The dense PbI_2 film and the volume expansion from PbI_2 (to PVSK make the MAI or FAI gas difficult to penetrate into the bottom PbI_2 layer, resulting in uncomplete conversion in HCVD based PVSK films.[33,34] The unreacted PbI_2 in the PSCs not only affects the photovoltaic performances but also negatively influences the operational stability.[35]

In this work, we have systematically investigated the HCVD-based perovskite films and solar cells with a particular focus on the ETL/PVSK interface and crystallization kinetics of perovskites (**Figure 1**). More specifically, we find that the oxygen loss of SnO_2 in the HCVD process increases the interface defect density and carrier recombination. Potassium sulfamate (H_2KNO_3S, we abbreviate as PS) serves as the bridge between ETL and PVSK, which not only compensates the oxygen loss of SnO_2 but also passivates the uncoordinated Pb^{2+} in the perovskite film. In addition, *N*-methylpyrrolidone (NMP) is introduced into the PbI_2 precursor to form the PbI_2•NMP adduct, which can modulate the nucleation of the PbI_2 films and lower the energy barrier for perovskite formation in the HCVD process, promoting the complete conversion of PbI_2 to perovskite with high crystallinity and large grain size. Furthermore, the seed assisted growth strategy is employed to control the kinetic of perovskite crystal growth, which greatly reduces the free energy for perovskite crystal growth and increases the grain size. These strategies lead to not only the improvement of efficiency but also the enhancement of stability. As a result, the small area solar cells (aperture area = 0.09 cm^2) exhibit a high efficiency of 21.98% with a stable output performance of 21.15%. Moreover, a PCE of 16.16% for 5 × 5 cm^2 and a PCE of 12.12% for 10 × 10 cm^2 solar modules are achieved with a

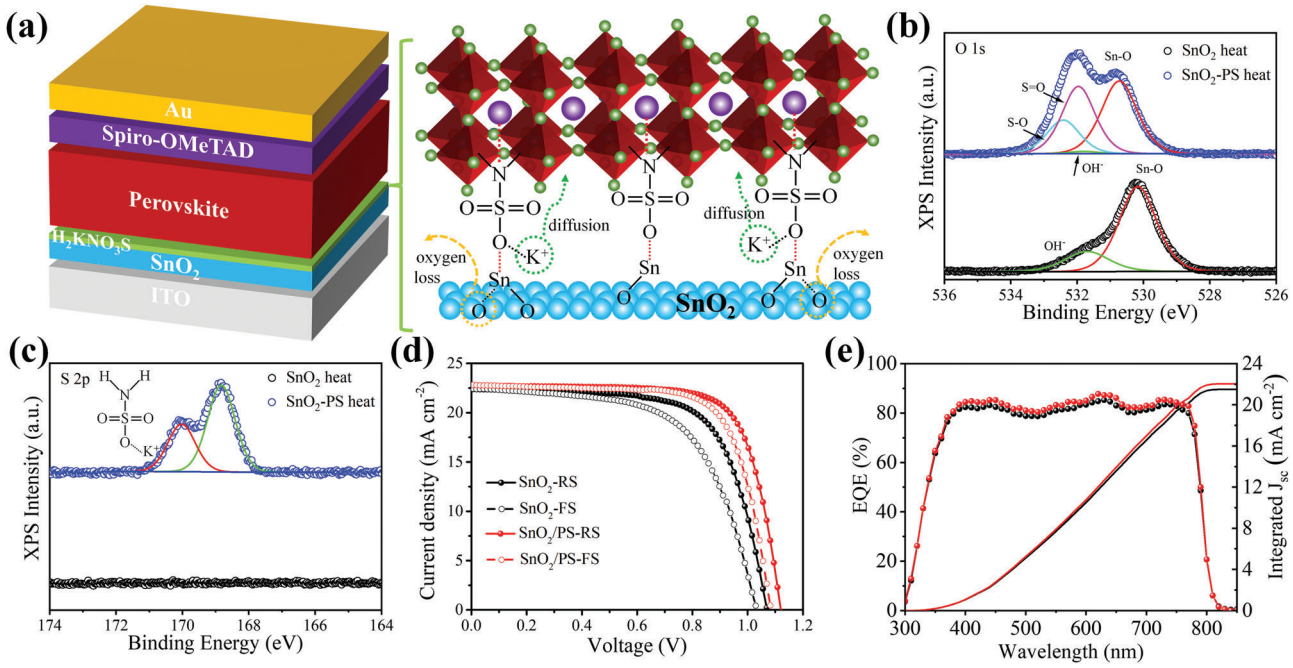

Figure 2. a) Schematic illustration of the ETL/PVSK interface passivation with H_2KNO_3S in the HCVD-based perovskite solar cell. b) O 1s, c) S 2p XPS spectra of SnO_2 and SnO_2/PS films under heat condition. d) *J–V* curves and e) EQE spectra of the HCVD-based perovskite solar cells with/without H_2KNO_3S passivation.

designated area of 22.4 and 91.8 cm^2, respectively. The 5 × 5 cm^2 solar module also shows a stable output performance of 14.72%. Remarkably, the small area PSCs and 5 × 5 cm^2 solar modules exhibit an excellent T_{80} operational stability lifetime over 4000 and 300 h, respectively, without any encapsulation under AM 1.5G continuous illumination at maximum power point in N_2 gas with a relative humidity of approximately 5%.

2. Results and Discussion

2.1. ETL/Perovskite Interface Modification

Figure 2a shows the PSCs with a configuration of ITO/SnO_2/H_2KNO_3S/perovskite/spiro-OMeTAD/Au, which features a thin layer of H_2KNO_3S deposited on top of SnO_2 followed by a post-annealing treatment. It is known that the uncoordinated Pb^{2+} ions in the perovskite serve as the trap centers, which increase the defect density in the devices. The amine group (–NH_2) in the H_2KNO_3S is expected to form bipolar bonds with the Pb^{2+} ion by sharing the electron with the empty orbitals of Pb^{2+}, which passivates the uncoordinated Pb^{2+} in the perovskites.[36,37] On the other hand, the K^+ ions in the H_2KNO_3S can diffuse into the perovskite layer, which has the similar function to other potassium ionic materials (i.e., ethylenediaminetetraacetic acid dipotassium salt [EDTAK], KOH, KCl, KFP_6) to reduce the hysteresis in the resultant devices and increase the grain size of perovskite films.[38–42] Furthermore, we anticipate that the continuous heating in the vacuum system in the HCVD process will create more oxygen vacancies in the SnO_2 films.[28,43] The presence of $[H_2NO_3S]^-$ ions on top of the SnO_2 ETL will connect with SnO_2 to passivate the oxygen vacancies. As illustrated in Figure 2a, H_2KNO_3S serves as a bridge between SnO_2 and the perovskite film to promote carrier transport and reduce the interface defects.

To verify our hypothesis, the surface property of the SnO_2 with/without H_2KNO_3S (PS) and with/without heating (hereafter labeled as SnO_2 RT/heat and SnO_2-PS RT/heat, respectively) were investigated using X-ray photoelectron spectroscopy (XPS) measurements. Here, RT means room temperature and heat indicates that the samples are heated (150 °C for 30 min, in vacuum), similar to the HCVD deposition process. From the XPS results in Figure 2b,c; Figures S1 and S2, Supporting Information (details of XPS analyses can be found in the Supporting Information), the atom ratio of O/Sn is 2.03 and 1.87 for SnO_2 film under RT and heat condition (Table S1, Supporting Information), respectively, which suggests the oxygen loss in the SnO_2 film occurs during the heat process in the vacuum system. As for the SnO_2-PS film, the existence of S 2p means the H_2KNO_3S is relatively stable under continuous heating in the vacuum system. On the other hand, the O/Sn atom ratio of 1.96 suggests that the oxygen vacancy is successfully passivated by H_2KNO_3S.

To understand the effect of H_2KNO_3S on the perovskite/SnO_2 interface, the steady-state photoluminescence (PL) and time-resolved photoluminescence (TRPL) measurements were performed. As seen in Figure S3, Supporting Information, the longer lifetime and improved PL intensity of perovskite/PS compared with the sample without PS suggests that the presence of PS can passivate the perovskite films and reduce the defects. On the contrary, the shorter lifetime and fluorescence quenching of the perovskite/SnO_2-PS sample compared with the perovskite/SnO_2 case indicates that fewer defects are observed at the SnO_2/perovskite interface, leading to fast carrier transport

and transfer. The lifespans of the perovskite films are fitted by a bi-exponential function. The corresponding lifetimes are summarized in Table S2, Supporting Information. Furthermore, the secondary ion mass spectrometry (SIMS) measurement is conducted to investigate the K^+ diffusion behavior. From Figure S4, Supporting Information, K^+ exists in the perovskite bulk film and H_2KNO_3S passivation layer, which not only passivates the defects in the perovskite film but also reduces the hysteresis of the resultant device.

The performance of the devices with/without H_2KNO_3S is shown in Figure S5 and Tables S3 and S4, Supporting Information. In combination with the H_2KNO_3S as a passivation layer and HCVD process, the efficiency of the devices increases considerably (Figure S6, Supporting Information). The efficiency of the champion device, treated with 10 mM H_2KNO_3S, is 18.81% (V_{oc} = 1.12 V, J_{sc} = 22.73 mA cm^{-2}, and FF = 0.74) with a hysteresis index (HI = PCE_{RS}/PCE_{FS}) of 1.06, while as a comparison, the control device shows a PCE of 16.25% (V_{oc} = 1.07 V, J_{sc} = 22.38 mA cm^{-2}, and FF = 0.68) with a HI of 1.15 (Figure 2d,e). Moreover, the average PCE of the device without H_2KNO_3S is only 14.88%, whereas the average PCE of the SnO_2/PS devices increase to 18.18%. To further demonstrate it, the similar procedures are conducted to fabricate the devices based on CBD-SnO_2 (chemical bath deposition, CBD). The pristine CBD-SnO_2 devices exhibit a large hysteresis, which has been demonstrated in our previous works.[44,45] By incorporating 10 mM H_2KNO_3S, the CBD-SnO_2/PS device exhibits a high efficiency of 22.44% (average PCE = 21.51% ± 0.68%) as seen in Figure S7, Supporting Information.

2.2. Nucleation and Growth of Perovskites

Besides the ETL/perovskite interface, the preparation of perovskites also has significant influence on the quality of a perovskite film. Lower crystallinity and smaller grain size of the perovskites substantially increase the density of grain boundaries, which increases the defect density in perovskite films, resulting in a low efficiency and inferior stability. Different from conventional solution processed perovskite deposition, HCVD provides a multiple-step deposition process, which indicates that the conversion from PbI_2 to perovskite is a key step in both nucleation and growth of the perovskites. Moreover, NMP has been demonstrated as an efficient additive in our previous work,[45,46] which can form a stable PbI_2•NMP adduct, promoting the process of nucleation and growth of perovskites. Here, the PbI_2 film fabricated by vapor deposition and spin-coating methods was investigated. To simplify the labeling, PbI_2 fabricated by vapor deposition and PbI_2 dissolved in DMF and DMF/NMP mixed solvent are abbreviated as PVD-PbI_2, DMF-PbI_2, and NMP-PbI_2, respectively. The corresponding perovskite films are abbreviated as PVD-PVSK, DMF-PVSK, and NMP-PVSK, respectively. As seen in Figure S8, Supporting Information, the PVD-PbI_2 film presents dark yellow color. However, the NMP-PbI_2 film shows a distinctive light-yellow color. To gain insight into the phase structure of PbI_2 films, X-ray diffraction (XRD) and scanning electron microscopy (SEM) were conducted and the results are displayed in **Figure 3**. Similar to the previous reports, the PVD-PbI_2 film presents the 2D-layered nanosheet structure with a strong intensity peak at 12.6°.[34] As a comparison, the DMF-PbI_2 film shows the sponge-like porous structure with a reduced peak intensity at 12.6°. Note that the appearance of peak at ≈8° instead of typical PbI_2 peak in NMP-PbI_2 film is ascribed to the formation of intermediate phase of PbI_2•NMP because of the strong binding between NMP and PbI_2.[45] After the MAI vapor deposition in the HCVD process, the PVD-PVSK and DMF-PVSK films show a surface morphology consisting of small grains. In contrast, the NMP-PVSK film presents high crystallinity, enlarged grain size with uniform distribution as seen in Figure 3f–h; Figure S9, Supporting Information. It is remarkable that the presence of the intermediate phase of PbI_2•NMP can greatly lower the energy barrier for perovskite nucleation, facilitating the conversion from PbI_2 to perovskite (Figure 3a). In contrast, a strong peak at 12.6° can be still observed in PVD-PVSK and DMF-PVSK films, which is presumably related to the unreacted PbI_2 in the MAI vapor deposition process.

To validate the nucleation mechanism in perovskites, we investigated the performance of perovskite solar cells. Statistical analyses of device parameters based on PVD-PVSK, DMF-PVSK, and NMP-PVSK methods are shown in Figure S10 and Tables S5 and S6, Supporting Information. The average efficiency for PVD-PVSK, DMF-PVSK, and NMP-PVSK based devices is 16.38%, 18.18%, and 19.23%, respectively. The champion current density–voltage (*J*–*V*) curves are shown in **Figure 4**a; Table S5, Supporting Information. The low PCE of 17.19% in the case of PVD-PVSK-based device is ascribed to the unreacted PbI_2 at the interface of ETL/PVSK, which prevents part of the light from going through this PbI_2 layer. By contrast, the high PCEs of 19.79% for NMP based device are the results of high crystallinity and large grain size of perovskites and less defects in the perovskite films in comparison with DMF-PVSK based devices (PCE = 18.81%), which is showing small grain size and low crystallinity. Moreover, the external quantum efficiency (EQE) of the NMP-PVSK based device in Figure 4b shows slightly higher values than the other two devices in the short wavelength regions ascribed to the completed conversion of PbI_2 to the perovskite phase. The high EQE values in long-wavelength indicate that high crystallinity of perovskite film not only increases the light harvesting efficiency but also reduces the carrier recombination due to traps in the devices. In addition, three devices exhibit stable output (under initial maximum power point (MPP) voltage) with PCE of 15.83%, 17.65%, and 19.20%, respectively (Figure 4c).

To gain further information, we used the space charge–limited current (SCLC) method to determine the trap density of the three perovskite films by constructing the hole-only devices (ITO/PEDOT:PSS/Perovskite/Au) and the electron-only devices (ITO/SnO_2/Perovskite/PCBM/Ag) (Figure 4e–g; Figure S11, Supporting Information). The trap density values of hole-only devices are 1.06 × 10^{16}, 8.73 × 10^{15}, and 7.71 × 10^{15} cm^{-3} for PVD-PVSK, DMF-PVSK, and NMP-PVSK films, respectively. The trap density values of electron-only devices are 4.57 × 10^{15}, 3.96 × 10^{15}, and 3.04 × 10^{15} cm^{-3} for PVD-PVSK, DMF-PVSK, and NMP-PVSK films, respectively. The decrease of trap density indicates that the presence of intermediate phase and low energy barrier for nucleation can considerably promote the growth of perovskite with high crystallinity, and reduce the defect density in the perovskite films. In addition, the longer lifetime

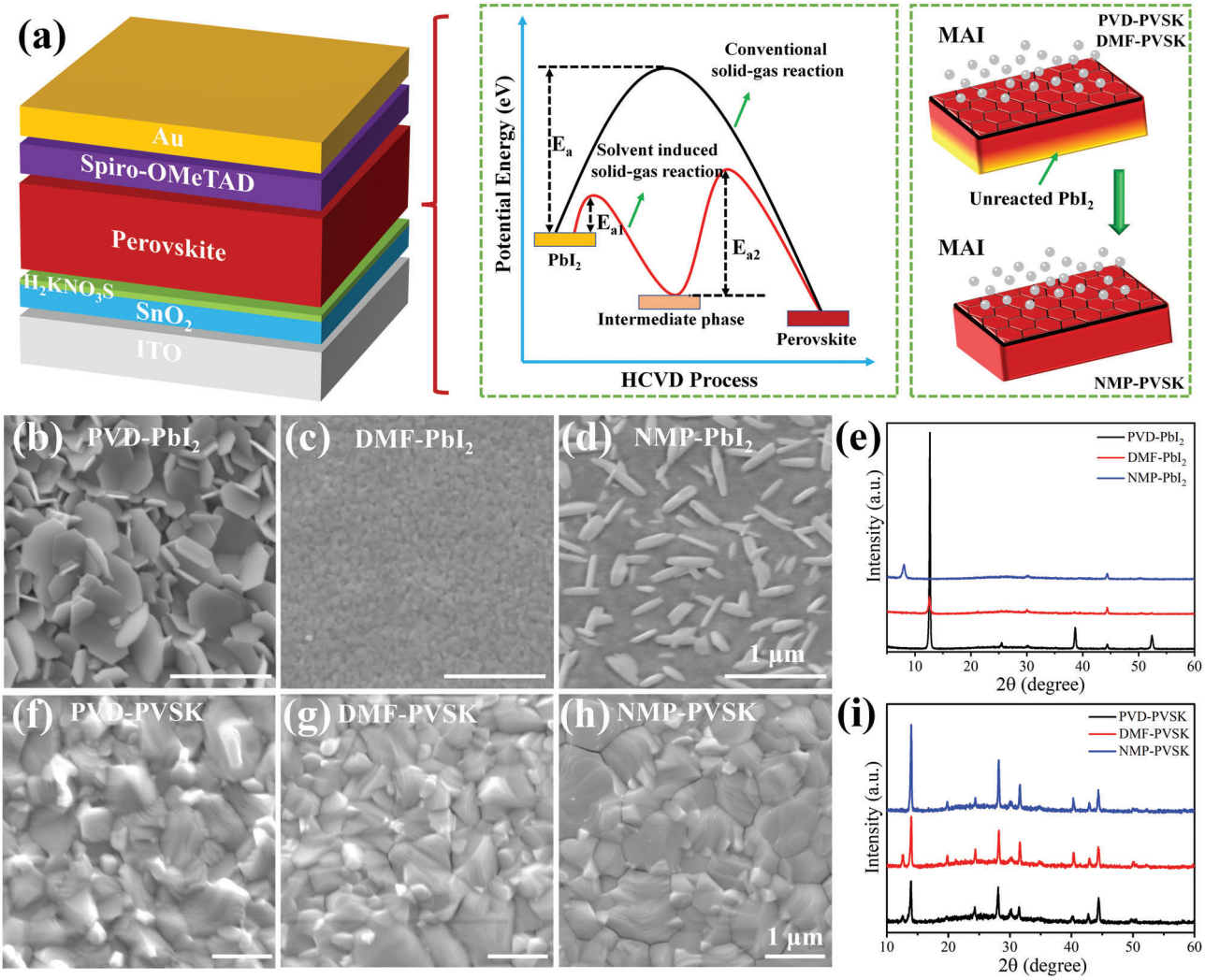

Figure 3. a) Schematic illustration of the nucleation and growth of perovskites in a HCVD-based perovskite solar cell. Top-view SEM images of b) PVD-PbI_2, c) DMF-PbI_2, and d) NMP-PbI_2. e) XRD patterns of PbI_2 processed with different methods. Top-view SEM images of the corresponding perovskite films are shown in f) PVD-PVSK, g) DMF-PVSK, and h) NMP-PVSK. i) XRD patterns of the perovskite films processed with the different methods.

and increased fluorescence intensity of NMP-PVSK film (Figure 4d; Figure S12 and Table S2, Supporting Information) also demonstrates that this film has less defects and better crystallinity than DMF-PVSK and PVD-PVSK films.

2.3. Seed Assisted Growth of Perovskite Crystals

Although the passivation of electron transport layer and the modulation of perovskite nucleation have greatly improved the performance of PSCs in the HCVD process, the efficiency of HCVD based solar cells still lags behind the conventional solution processed devices. One of the important issues is that the grain size of HCVD based perovskite films is smaller than that of conventional solution processed perovskite films. It has been widely accepted that the crystallization of perovskites will not occur until the formation of nuclei in the sequential deposition.[47] As seen in **Figure 5**, the MAI vapor diffusion induces instant supersaturation at the top of PbI_2 layer (conventional perovskite sample, black curve), which enables to overcome the high energy barrier, leading to nucleation of the perovskites. Inspired by previous reports that the perovskite seeds can greatly modulate the crystallization kinetics,[47,48] the seed layer was deposited on the substrate and then exposed to MAI vapor in HCVD system (more details can be found in the Supporting information). Here, the PbI_2 film that has partially reacted with FAI is labeled as Seed. The perovskite film fabricated by depositing MAI on top of the seed layer is named as Seed-PVSK. Different from perovskite films showing large grain size, the seed layer contains plenty of small grains. Moreover, the strong XRD patterns at ≈12.6° and ≈14° assigned to PbI_2 and perovskite phase, respectively, indicate that the seed layer includes two phases (Figure 5c,e). After MAI deposition, the unreacted PbI_2 phase fully converts to perovskite. The resultant perovskite film presents dense, uniform distribution, and large grain sizes with over one-micrometer (Figure 5d,e). The high quality and large grain size perovskite film is related to the

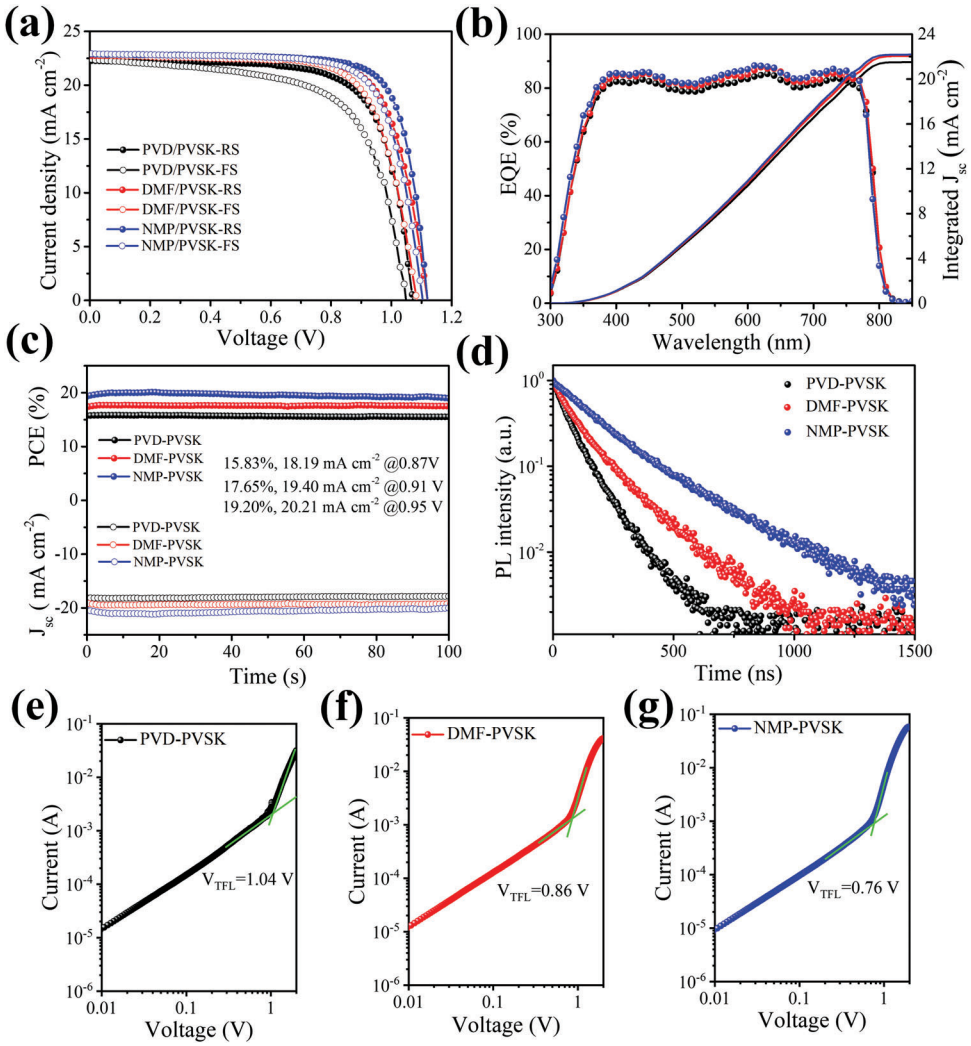

Figure 4. a) *J–V* curves of the PSCs based on different methods. b) The corresponding EQE spectra. c) The steady-state power output performance of the PSCs based on different methods. d) TRPL decay curves of the perovskite films based on different methods on the glass substrates. Dark *I–V* characteristics of the devices with the ITO/PEDOT:PSS/perovskite/Au configuration of e) PVD-PVSK, f) DMF-PVSK, and g) NMP-PVSK.

fact that the perovskite seed acts as the nucleation center, which greatly reduces the formation energy barrier and increases the kinetics of the perovskite crystal growth. (Figure 5b, red curve). In addition, the presence of seed creates PbI_2/perovskite interface channels that facilitate the diffusion and intercalation of MAI cations and halide anions into the bottom PbI_2, promoting the grain growth and yielding a large grain size (Figure 5a).[47]

The solar cells were fabricated to evaluate the quality of perovskite films fabricated by the seed assisted growth method. First, we investigated the seed-based solar cells. It was found that the perovskite seed as the absorber layer in the solar cells yielded an average PCE of 14.72% (Figure S13 and Table S7, Supporting Information), which is ascribed to the small amount of perovskite in the Seed layer. However, the Seed-PVSK as the absorber layer presented a high performance with an average PCE of 20.59% (Figure S13, Table S7, Supporting Information). The resultant champion efficiency was 21.98% (Figure 5f; Figure S14 and Table S8, Supporting Information) with a steady-state power output performance of 21.15%, which is the highest efficiency for the HCVD-based PSCs (Tables S9 and S10, Supporting Information). In comparison with the NMP-PVSK device, the improved performance of Seed-PVSK device is ascribed to the reduced formation energy barrier that facilitates the continuous growth of perovskite grains, leading to large grain size (Figure S15, Supporting Information) and reduced trap defects. The enhanced EQE (Figure 5g) at short and long wavelength is probably attributed to the good crystallinity of the perovskite film, the reduced unreacted PbI_2, and interface defects at the ETL/PVSK interface.

To further identify the reduced defects and understand the carrier transport behavior, we evaluated the surface potential of perovskite films by Kelvin probe force microscopy (KPFM). As seen in Figure S16, Supporting Information, the Seed-PVSK shows large grain sizes and uniform distribution, which leads to a smooth surface with a root-mean-square roughness (RMS) of 24.64 nm in comparison with NMP-PVSK case showing a RMS value of 42.92 nm. Moreover, the surface potential map-

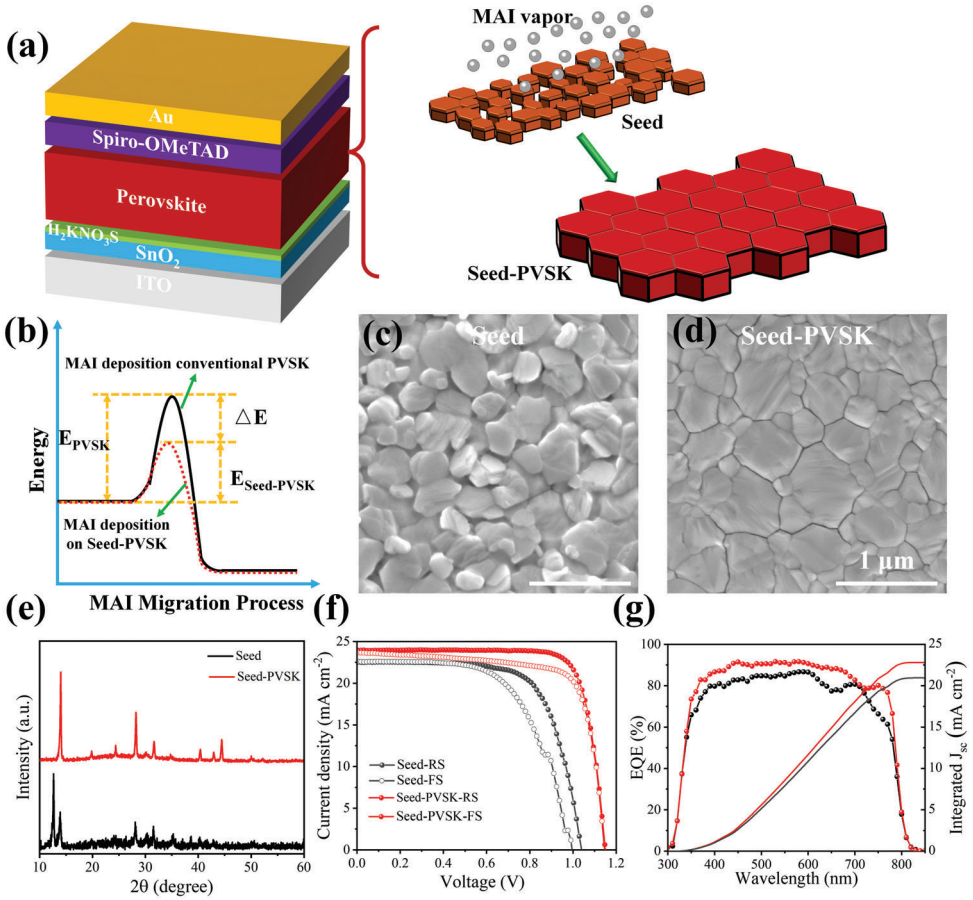

Figure 5. a) Schematic illustration of the seed growth of perovskites. b) Proposed energy diagram of MAI diffusion in the HCVD process. c,d) Top-view SEM images and e) XRD patterns of seed and seed-PVSK films. f) *J–V* curves and g) EQE spectra of the Seed and Seed-PVSK devices. Note that here the PbI_2 film reacting with partial FAI is named as Seed. The perovskite film fabricated by depositing MAI on the top of the Seed layer is named as Seed-PVSK.

pings of Seed-PVSK and NMP-PVSK are displayed in Figure S16, Supporting Information. Note that the Seed-PVSK film presents the lower average surface potential and reduced energy potential barrier between the grain boundaries and perovskite crystals in comparison with NMP-PVSK case, which is expected to remarkably promote the carrier transport.[19] In addition, the longer lifetime and increased fluorescence intensity also demonstrate the improved quality and reduced defects in the Seed-PVSK film (Figures S12 and S17, Supporting Information; and Table S2, Supporting Information).

2.4. Up-Scalable Perovskite Solar Modules and Operational Stability

To highlight the up-scalability of both HCVD process and our systematic modification, we fabricated relatively large-area PSMs on 5 × 5 cm^2 substrates with the similar structures as employed in small area device (**Figure 6**). The 5 × 5 cm^2 PSM consists of seven sub-cells in series with a designated area of 22.4 cm^2 (Figure S18, Supporting Information). The sub-cells are separated by P1, P2, and P3 patterns (Figure S19, Supporting Information). The PCEs of the PSMs fabricated by the above-mentioned systematic modification of HCVD process range from ≈13–16% with an average PCE of 15.01% (Table S11 and Figure S20, Supporting Information). The champion PCE of 5 × 5 cm^2 PSM is 16.16% with a V_{oc} of 7.82 V, a J_{sc} of 2.91 mA cm^{-2}, and a FF of 0.71 for the reverse scan (RS) and the PCE of 13.87% for the forward scan (FS). The corresponding active area efficiency of the champion PSM is up to 17.15% with a geometric fill factor (GFF) of 94% (Figure S18, Supporting Information). Moreover, the PSM exhibits a stable efficiency of 14.72% (Figure S21, Supporting Information). In contrast, the PCE of PSM fabricated without modification ranges from ≈8–12%, with an average PCE of 10.89%. The corresponding champion PCE is only 12.31% (Table S12 and Figure S20, Supporting Information). Note that the hysteresis in the large-area solar modules is more severe than that of the small-area solar cells, which is mainly induced by the increased size of the devices. As the size increases, the number of bulk and/or surface defects increases, and also ion migration and imbalanced carrier transport become more prominent, which will lead to an increased hysteresis in comparison with small area solar cells.[49,50] Besides, to further demonstrate the scalability of our process, we fabricated a relatively larger mini-module on 10 × 10 cm^2

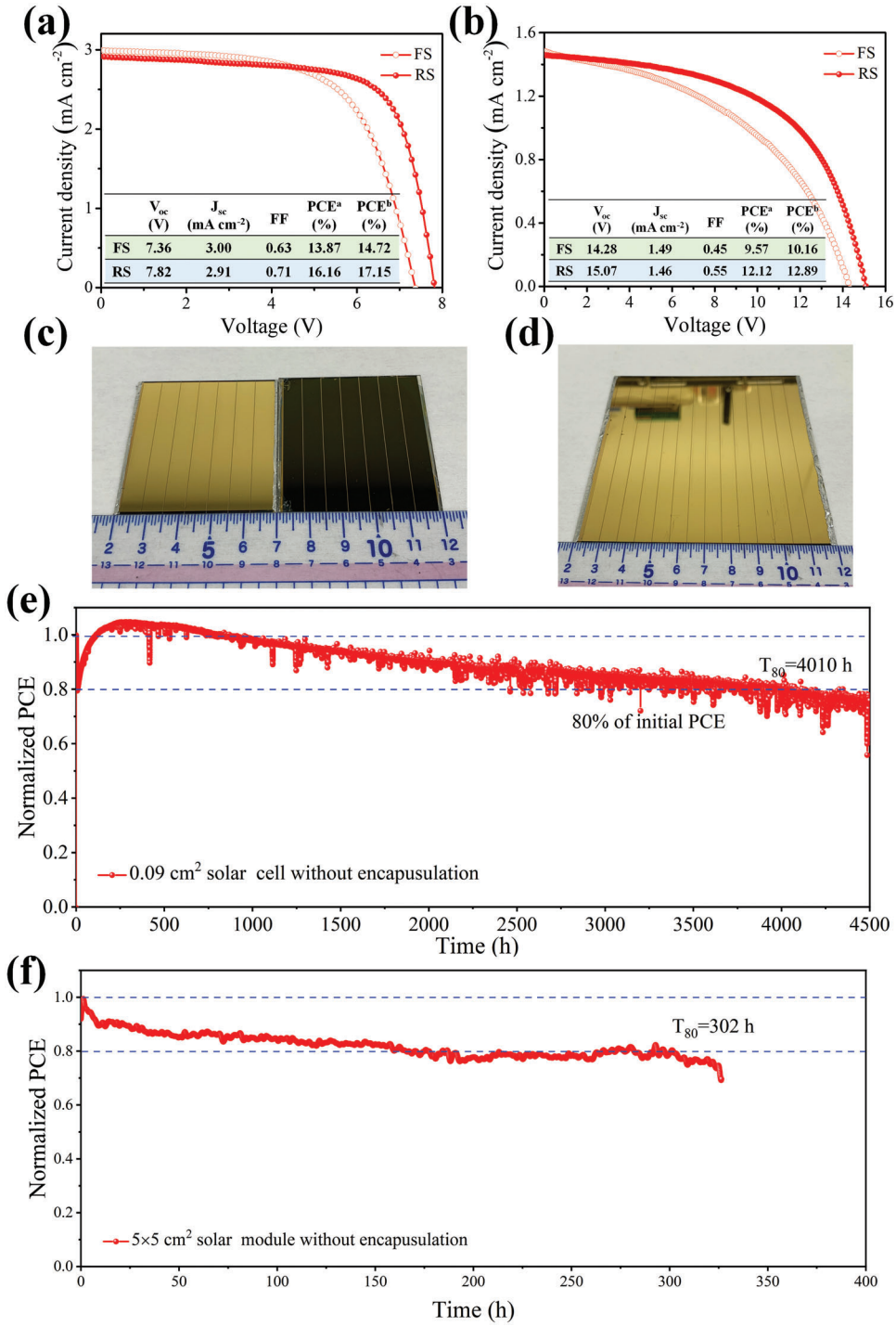

Figure 6. *J–V* curves of a) 5 × 5 cm^2 PSM and b) 10 × 10 cm^2 PSM. Photos of c) 5 × 5 cm^2 PSM and d) 10 × 10 cm^2 PSM. Operational stability of e) the small-area PSC and f) the 5 × 5 cm^2 PSM without encapsulation under a steady applied voltage corresponding to the initial maximum power point.

substrates consisting of 14 sub-cells in series with a designed area of 91.8 cm^2. The PCE ranges from ≈9–12% with an average PCE of 10.72% (Table S13 and Figure S22, Supporting Information) and the highest PCE of 10 × 10 cm^2 PSM is 12.12% under RS. The corresponding active area efficiency is up to 12.88% with a GFF of 94% (Figure S23, Supporting Information).

Last, the operational stability of unencapsulated PSCs and PSM were evaluated under continuous AM 1.5G light illumination at a fixed bias that was determined by the initial MPP from *J–V* characterizations (in N_2 gas with relative humidity of 5% at room temperature, Figure 6e,f). For the small area PSC, it exhibited an outstanding operational stability and kept 90%

of the initial performance after 1700 h. Remarkably, the T_{80} lifetime of small area device is ≈4010 h. The improved stability of PSCs is ascribed to the following reasons: i) The unreacted PbI_2 phase in perovskite film is reduced after MAI deposition by the HCVD process. The excess/unreacted PbI_2 in the PSCs undergoes the photodecomposition under continuous illumination, which greatly promotes the formation of lead and iodine in PSCs, leading to accelerating the degradation of device performance.[35,51] Here, the unreacted PbI_2 is eliminated as seen in Figure 3i and Figure 5e by the formation of PbI_2•NMP intermediate phase and seed assisted growth because of the reduced phase transition energy, which increases the stability of PSCs. ii) The improved crystallinity and enlarged grain size in the perovskite film also improves the stability. The existence of stress and ion migration in the perovskite film will accelerate the decomposition of perovskite, which starts from grain boundaries (GBs).[34,40] Note that the seed-PVSK shows large grain size, less GBs, and low surface potential, which reduces the degradation kinetics compared with other samples presenting small grain size and large amounts of GBs, leading to an improved stability.

In addition, the 5×5 cm^2 PSM also shows an operational stability with a T_{80} lifespan of 302 h. It is worth noting that the reduction in operation stability between large area module and small area solar cells is ascribed to the size increase of devices. During the operation stability test, the perovskite solar modules generate heat and long-term light illumination also contributes to the temperature increase. Therefore, the temperature of solar modules rises to the temperature that is substantially higher than that in the case of small area solar cells. The increased temperature in the solar module accelerates the degradation of hole transport layer, leading to the poor operation lifetime of solar modules in comparison with small area solar cells. Moreover, as the size of the solar modules increases, the light induced photocatalytic degradation from electron transport layer and ion migrations originating from light illumination becomes more prominent,[52] which also speed ups the degradation of devices, resulting in the poorer operation stability of solar modules in comparison with the small area solar cells.

3. Conclusion

In conclusion, we have demonstrated an efficient strategy to fabricate perovskite solar cells/modules via a HCVD method that relies on the ETL modification and control of the solid–gas reaction. The presence of H_2KNO_3S serves as the bridge between ETL and perovskite film, which not only compensates the oxygen loss of SnO_2 but also passivates the uncoordinated Pb^{2+} in the perovskite. Moreover, the use of NMP as the additive solvent is expected to form the intermediate phase of PbI_2•NMP that greatly lowers the solid–gas reaction energy and promotes the full conversion from PbI_2 to perovskite. Furthermore, the perovskite seed assisted growth method is introduced to control the kinetics of perovskite crystal growth and increase the perovskite grain size. On the basis of the systematic research, a champion efficiency of 21.98% (stable output performance of 21.15%) was achieved for lab-scale solar cells (aperture area = 0.09 cm^2). To demonstrate the scalability of our HCVD process, the mini-modules fabricated on 5×5 cm^2 and 10×10 cm^2 substrates achieved an efficiency of 16.16% (stable output performance of 14.72%) and 12.12% with a designated area of 22.4 cm^2 and 91.8 cm^2, respectively. Moreover, the unencapsulated small area solar cell showed an excellent operational stability and retained ≈80% of the initial performance for ≈4010 h under AM1.5G continuous light illumination (at maximum power point, in N_2 gas with 5% relative humidity, at room temperature). Our research demonstrates a significant step forward in the development of the HCVD-based perovskite solar cells/modules.

Supporting Information

Supporting Information is available from the Wiley Online Library or from the author.

Acknowledgements

This work was supported by funding from the Energy Materials and Surface Sciences Unit of the Okinawa Institute of Science and Technology Graduate University, the OIST R & D Cluster Research Program, the OIST Proof of Concept (POC) Program, JST A-STEP Grant Number JPMJTM20HS, and JSPS KAKENHI Grant Number JP21F21754. The authors thank the OIST Micro/Nanofabrication Section and Imaging Section for the support. G.T. thanks the research startup grant by Hefei University of Technology, Anhui innovation and entrepreneurship support plan for Returned Overseas Students (no. 2022LCX018).

Conflict of Interest

The authors declare no conflict of interest.

Author Contributions

G.T. and J.Z. contributed equally to this work. Y.B.Q. supervised this research project. G.T., J.Z., and Y.B.Q. conceived the research ideas, performed the data analysis, and wrote the draft manuscript. G.T., J.Z., L.K.O., and Y.B.Q. participated in the discussion about the experimental details. G.T. and J.Z. conducted the solar cell fabrication and the characterization including XRD, SEM, AFM, *J–V* measurements, and stability tests. G.T. and L.K.O. performed XPS and SIMS measurements. T.B. helped with the solar module fabrication. C.Z. helped with the PL and TRPL measurements. S.M. and S.K. helped with the *J–V* measurements of the solar cell devices. Y.L., C.D., and T.W. helped with the sample preparation for characterization and provided suggestions on the experiments. All authors contributed to revisions of the manuscript.

Data Availability Statement

The data that support the findings of this study are available from the corresponding author upon reasonable request.

Keywords

chemical vapor deposition, grain growth, nucleation, perovskite solar modules, SnO_2

Received: January 15, 2023
Revised: March 18, 2023
Published online: April 14, 2023

[1] H. Min, D. Y. Lee, J. Kim, G. Kim, K. S. Lee, J. Kim, M. J. Paik, Y. K. Kim, K. S. Kim, M. G. Kim, T. J. Shin, S. Il Seok, *Nature* **2021**, *598*, 444.
[2] F. Huang, M. Li, P. Siffalovic, G. Cao, J. Tian, *Energy Environ. Sci.* **2019**, *12*, 518.
[3] J. Yang, E. L. Lim, L. Tan, Z. Wei, *Adv. Energy Mater.* **2022**, *12*, 2200975.
[4] https://www.nrel.gov/pv/assets/pdfs/best-research-cell-efficiencies-rev220630.pdf **2022**.
[5] S. Wang, P. Wang, B. Chen, R. Li, N. Ren, Y. Li, B. Shi, Q. Huang, Y. Zhao, M. Grätzel, X. Zhang, *eScience* **2022**, *2*, 339.
[6] W. Shao, H. Wang, F. Ye, C. Wang, C. Wang, H. Cui, K. Dong, Y. Ge, T. Wang, W. Ke, G. Fang, *Energy Environ. Sci.* **2023**, *16*, 138.
[7] J. He, W. Sheng, J. Yang, Y. Zhong, Y. Su, L. Tan, Y. Chen, *Energy Environ. Sci.* **2023**, *16*, 629.
[8] H. Zhang, N.-G. Park, *eScience* **2022**, *2*, 567.
[9] Y. Zhu, P. Lv, M. Hu, S. R. Raga, H. Yin, Y. Zhang, Z. An, Q. Zhu, G. Luo, W. Li, F. Huang, M. Lira-Cantu, Y. B. Cheng, J. Lu, *Adv. Energy Mater.* **2023**, *13*, 202203681.
[10] M. Liu, M. B. Johnston, H. J. Snaith, *Nature* **2013**, *501*, 395.
[11] M. Roß, S. Severin, M. B. Stutz, P. Wagner, H. Köbler, M. Favin-Lévêque, A. Al-Ashouri, P. Korb, P. Tockhorn, A. Abate, B. Stannowski, B. Rech, S. Albrecht, *Adv. Energy Mater.* **2021**, *11*, 2101460.
[12] K. B. Lohmann, S. G. Motti, R. D. J. Oliver, A. J. Ramadan, H. C. Sansom, Q. Yuan, K. A. Elmestekawy, J. B. Patel, J. M. Ball, L. M. Herz, H. J. Snaith, M. B. Johnston, *ACS Energy Lett.* **2022**, *7*, 1903.
[13] H. Li, L. Tan, C. Jiang, M. Li, J. Zhou, Y. Ye, Y. Liu, C. Yi, *Adv. Funct. Mater.* **2022**, *33*, 2211232.
[14] Felix U. Kosasih, E. Erdenebileg, N. Mathews, S. G. Mhaisalkar, A. Bruno, *Joule* **2022**, *6*, 2692.
[15] L. Gil-Escrig, C. Dreessen, F. Palazon, Z. Hawash, E. Moons, S. Albrecht, M. Sessolo, H. J. Bolink, *ACS Energy Lett.* **2021**, *6*, 827.
[16] T. Abzieher, T. Feeney, F. Schackmar, Y. J. Donie, I. M. Hossain, J. A. Schwenzer, T. Hellmann, T. Mayer, M. Powalla, U. W. Paetzold, *Adv. Funct. Mater.* **2021**, *31*, 2104482.
[17] M. Wang, P. Zeng, S. Bai, J. Gu, F. Li, Z. Yang, M. Liu, *Sol. RRL* **2018**, *2*, 1800217.
[18] T. Chen, G. Tong, E. Xu, H. Li, P. Li, Z. Zhu, J. Tang, Y. B. Qi, Y. Jiang, *J. Mater. Chem. A* **2019**, *7*, 20597.
[19] G. Tong, T. Chen, H. Li, L. Qiu, Z. Liu, Y. Dang, W. Song, L. K. Ono, Y. Jiang, Y. B. Qi, *Nano Energy* **2019**, *65*, 104015.
[20] H. Li, J. Zhou, L. Tan, M. Li, C. Jiang, S. Wang, X. Zhao, Y. Liu, Y. Zhang, Y. Ye, W. Tress, C. Yi, *Sci. Adv.* **2022**, *8*, eabo7422.
[21] J. Feng, Y. Jiao, H. Wang, X. Zhu, Y. Sun, M. Du, Y. Cao, D. Yang, S. Liu, *Energy Environ. Sci.* **2021**, *14*, 3035.
[22] G. Tong, H. Li, G. Li, T. Zhang, C. Li, L. Yu, J. Xu, Y. Jiang, Y. Shi, K. Chen, *Nano Energy* **2018**, *48*, 536.
[23] M. R. Leyden, L. K. Ono, S. R. Raga, Y. Kato, S. Wang, Y. B. Qi, *J. Mater. Chem. A* **2014**, *2*, 18742.
[24] L. Qiu, S. He, Y. Jiang, Y. B. Qi, *J. Mater. Chem. A* **2021**, *9*, 22759.
[25] H. Li, M. Liu, M. Li, H. Park, N. Mathews, Y. B. Qi, X. Zhang, H. J. Bolink, K. Leo, M. Graetzel, C. Yi, *iEnergy* **2022**, *1*, 434.
[26] Y. Jiang, S. He, L. Qiu, Y. Zhao, Y. B. Qi, *Appl. Phys. Rev.* **2022**, *9*, 22759.
[27] T. D. L. A. A. U. Ebong, *Renewable Sustainable Energy Rev.* **2017**, *70*, 1286.
[28] L. Qiu, S. He, Y. Jiang, D.-Y. Son, L. K. Ono, Z. Liu, T. Kim, T. Bouloumis, S. Kazaoui, Y. B. Qi, *J. Mater. Chem. A* **2019**, *7*, 6920.
[29] J. Li, H. Wang, X. Y. Chin, H. A. Dewi, K. Vergeer, T. W. Goh, J. W. M. Lim, J. H. Lew, K. P. Loh, C. Soci, T. C. Sum, H. J. Bolink, N. Mathews, S. Mhaisalkar, A. Bruno, *Joule* **2020**, *4*, 1035.
[30] L. Qiu, L. K. Ono, Y. Jiang, M. R. Leyden, S. R. Raga, S. Wang, Y. B. Qi, *J. Phys. Chem. B* **2018**, *122*, 511.
[31] C. Zhang, H. Wang, H. Li, Q. Zhuang, C. Gong, X. Hu, W. Cai, S. Zhao, J. Chen, Z. Zang, *J. Energy Chem.* **2021**, *63*, 452.
[32] B. Tu, Y. Shao, W. Chen, Y. Wu, X. Li, Y. He, J. Li, F. Liu, Z. Zhang, Y. Lin, X. Lan, L. Xu, X. Shi, A. M. C. Ng, H. Li, L. W. Chung, A. B. Djurisic, Z. He, *Adv. Mater.* **2019**, *31*, 1805944.
[33] T. Zhang, M. Yang, Y. Zhao, K. Zhu, *Nano Lett.* **2015**, *15*, 3959.
[34] G. Tong, D. Y. Son, L. K. Ono, Y. Liu, Y. Hu, H. Zhang, A. Jamshaid, L. Qiu, Z. Liu, Y. B. Qi, *Adv. Energy Mater.* **2021**, *11*, 2003712.
[35] G. Tumen-Ulzii, C. Qin, D. Klotz, M. R. Leyden, P. Wang, M. Auffray, T. Fujihara, T. Matsushima, J. W. Lee, S. J. Lee, Y. Yang, C. Adachi, *Adv. Mater.* **2020**, *32*, 1905035.
[36] T. Singh, S. Öz, A. Sasinska, R. Frohnhoven, S. Mathur, T. Miyasaka, *Adv. Funct. Mater.* **2018**, *28*, 1706287.
[37] C. Tian, K. Lin, J. Lu, W. Feng, P. Song, L. Xie, Z. Wei, *Small Methods* **2019**, *4*, 1900476.
[38] D. Y. Son, S. G. Kim, J. Y. Seo, S. H. Lee, H. Shin, D. Lee, N. G. Park, *J. Am. Chem. Soc.* **2018**, *140*, 1358.
[39] P. Zhu, S. Gu, X. Luo, Y. Gao, S. Li, J. Zhu, H. Tan, *Adv. Energy Mater.* **2019**, *10*, 1903083.
[40] Z. Liu, L. Qiu, L. K. Ono, S. He, Z. Hu, M. Jiang, G. Tong, Z. Wu, Y. Jiang, D.-Y. Son, Y. Dang, S. Kazaoui, Y. B. Qi, *Nat. Energy* **2020**, *5*, 596.
[41] Z. Wang, T. Wu, L. Xiao, P. Qin, X. Yu, L. Ma, L. Xiong, H. Li, X. Chen, Z. Wang, T. Wu, M. L. Xiao, P. Qin, D. X. Yu, D. L. Ma, D. L. Xiong, D. H. Li, X. Chen, *J. Power Sources* **2021**, *488*, 229451.
[42] T. Bu, J. Li, F. Zheng, W. Chen, X. Wen, Z. Ku, Y. Peng, J. Zhong, Y. B. Cheng, F. Huang, *Nat. Commun.* **2018**, *9*, 4609.
[43] L. Qiu, Z. Liu, L. K. Ono, Y. Jiang, D. Y. Son, Z. Hawash, S. He, Y. B. Qi, *Adv. Funct. Mater.* **2018**, *29*, 1806779.
[44] G. Tong, L. K. Ono, Y. Liu, H. Zhang, T. Bu, Y. B. Qi, *Nano-Micro Lett.* **2021**, *13*, 155.
[45] T. Bu, J. Li, H. Li, C. Tian, J. Su, G. Tong, L. K. Ono, C. Wang, Z. Lin, N. Chai, X. L. Zhang, J. Chang, J. Lu, J. Zhong, W. Huang, Y. B. Qi, Y. B. Cheng, F. Huang, *Science* **2021**, *372*, 1327.
[46] T. Bu, L. K. Ono, J. Li, J. Su, G. Tong, W. Zhang, Y. Liu, J. Zhang, J. Chang, S. Kazaoui, F. Huang, Y.-B. Cheng, Y. B. Qi, *Nat. Energy* **2022**, *7*, 528.
[47] Y. Zhao, H. Tan, H. Yuan, Z. Yang, J. Z. Fan, J. Kim, O. Voznyy, X. Gong, L. N. Quan, C. S. Tan, J. Hofkens, D. Yu, Q. Zhao, E. H. Sargent, *Nat. Commun.* **2018**, *9*, 1607.
[48] Q. Li, Y. Zhao, R. Fu, W. Zhou, Y. Zhao, X. Liu, D. Yu, Q. Zhao, *Adv. Mater.* **2018**, *30*, 1803095.
[49] P. Liu, W. Wang, S. Liu, H. Yang, Z. Shao, *Adv. Energy Mater.* **2019**, *9*, 1803017.
[50] D.-H. Kang, N.-G. Park, *Adv. Mater.* **2019**, *31*, 1805214.
[51] Y. Zhao, F. Ma, Z. Qu, S. Yu, T. Shen, H. Deng, X. Chu, X. Peng, Y. Yuan, X. Zhang, J. You, *Science* **2022**, *377*, 531.
[52] J. Zhou, Y. Gao, Y. Pan, F. Ren, R. Chen, X. Meng, D. Sun, J. He, Z. Liu, W. Chen, *Sol. RRL* **2022**, *6*, 2200772.